

Insights into Kinesin-1 Stepping from Simulations and Tracking of Gold Nanoparticle-Labeled Motors

Keith J. Mickolajczyk,^{1,2} Annan S. I. Cook,^{1,3} Janak P. Jevtha,¹ John Fricks,⁴ and William O. Hancock^{1,2,*}

¹Department of Biomedical Engineering; ²Intercollege Graduate Degree Program in Bioengineering; ³Department of Physics, Pennsylvania State University, University Park, Pennsylvania; and ⁴School of Mathematical and Statistical Sciences, Arizona State University, Tempe, Arizona

ABSTRACT High-resolution tracking of gold nanoparticle-labeled proteins has emerged as a powerful technique for measuring the structural kinetics of processive enzymes and other biomacromolecules. These techniques use point spread function (PSF) fitting methods borrowed from single-molecule fluorescence imaging to determine molecular positions below the diffraction limit. However, compared to fluorescence, gold nanoparticle tracking experiments are performed at significantly higher frame rates and utilize much larger probes. In the current work, we use Brownian dynamics simulations of nanoparticle-labeled proteins to investigate the regimes in which the fundamental assumptions of PSF fitting hold and where they begin to break down. We find that because gold nanoparticles undergo tethered diffusion around their anchor point, PSF fitting cannot be extended to arbitrarily fast frame rates. Instead, camera exposure times that allow the nanoparticle to fully populate its stationary positional distribution achieve a spatial averaging that increases fitting precision. We furthermore find that changes in the rotational freedom of the tagged protein can lead to artifactual translations in the fitted particle position. Finally, we apply these lessons to dissect a standing controversy in the kinesin field over the structure of a dimer in the ATP waiting state. Combining new experiments with simulations, we determine that the rear kinesin head in the ATP waiting state is unbound but not displaced from its previous microtubule binding site and that apparent differences in separately published reports were simply due to differences in the gold nanoparticle attachment position. Our results highlight the importance of gold conjugation decisions and imaging parameters to high-resolution tracking results and will serve as a useful guide for the design of future gold nanoparticle tracking experiments.

SIGNIFICANCE Tracking protein dynamics by attaching a nanoparticle to the protein and tracking the dynamics of the particle is a widely used approach in single-molecule biophysics. However, with increasing spatiotemporal resolution, it is important to understand the relationship between the position of the actual protein and the measured position of the nanoparticle. Here, we use simulations to understand tethered particle dynamics, and we carry out single-molecule experiments on kinesin motor proteins in which one head is labeled at different positions by a gold nanoparticle. Through our experiments and simulations, we resolve a conflict in the literature, and we describe best practices for design and analysis of nanoparticle tracking experiments.

INTRODUCTION

Single-molecule imaging has revolutionized the study of biomacromolecules, allowing for the direct observation of behaviors invisible at the ensemble level (1,2). Pioneering work toward breaking the diffraction limit of light led to the idea of nanometer-scale single-molecule localization

by fitting to the emission profile of point source fluorophores (3–8), an idea now at the heart of multiple super-resolution techniques. In the molecular motor field, this early work spawned the Fluorescence Imaging with One Nanometer Accuracy technique, in which the point spread function (PSF) of a single fluorophore imaged under total internal reflection fluorescence microscopy is fit with a two-dimensional (2D) Gaussian to determine the particle center position (9–12). Collecting ~10,000 photons per 500 ms acquisition, the Selvin Lab used the Fluorescence Imaging with One Nanometer Accuracy technique to measure the discrete step sizes of myosin and kinesin motor proteins as they walked along cytoskeletal filaments, work that

Submitted September 19, 2018, and accepted for publication June 10, 2019.

*Correspondence: wohbio@engr.psu.edu

Keith J. Mickolajczyk and Annan S.I. Cook contributed equally to this work.

Editor: David Warshaw.

<https://doi.org/10.1016/j.bpj.2019.06.010>

© 2019 Biophysical Society.



immediately informed the mechanisms by which these motors stepped (9,10).

For PSF fitting, there is a trade-off between localization precision and temporal resolution that must be foremost in the mind of the experimenter. The standard error of the mean position determined by the Gaussian fitting method has been shown theoretically and experimentally to be proportional to $1/\sqrt{N}$, where N is the number of photons collected (13). Hence, as the camera exposure time is decreased to increase the frame rate, the localization precision decreases because of fewer photons being collected. Many proteins such as molecular motors undergo conformational changes at 100 Hz or faster (14–16), meaning that exposure times of 5 ms or less are necessary for proper sampling. The limited photon flux of organic dyes means that N will be too low at 5 ms exposure to achieve \sim 1-nm precision, limiting the effectiveness of PSF fitting in these applications.

To address the limitations of total internal reflection fluorescence microscopy-based PSF fitting, new techniques with higher effective photon fluxes were sought out. Significant success was achieved by switching from fluorescent probes to scattering probes, typically gold nanoparticles. In 2001, Yasuda et al. used dark field microscopy to image the rotations of F1-ATPase labeled with a 40-nm gold nanoparticle at 8000 frames per second, opening a new frontier in fast, precise single-molecule tracking (17). Subsequently, two techniques were developed, total internal reflection dark field microscopy (TIRDFM) (18–22) and interferometric scattering microscopy (23–27), which were able to achieve 1-nm localization precision with exposure times in the microsecond regime. These new techniques have allowed for fast, single-molecule kinetics to be measured for various nanoparticle-labeled biomacromolecules and have been used to verify and quantify previously undetectable structural intermediates (15,28–34). However, TIRDFM and interferometric scattering microscopy both ultimately rely on the same Gaussian fitting procedure developed for fluorescence, bringing back into question the assumptions of PSF fitting in the context of relatively large probes and sub-ms camera exposure times.

An investigation into the assumptions of PSF fitting for scattering-based single-molecule methods is particularly relevant to the kinesin field, in which a recent conflict has emerged on the structure of the ATP waiting state based on gold nanoparticle tracking data. In our own lab, stepping traces generated by tagging a single kinesin head with gold showed an ATP waiting state that was not detectably different from the two heads-bound state (15). Similar tracking from the Tomishige Lab showed an ATP waiting state with one head free and rapidly diffusing with a rightward bias (28). It has remained unknown whether the different tracking results are due to differences in the kinesin constructs, gold conjugation methods, buffer conditions, microscope types or settings, or some other source.

In this work, we use Brownian dynamics (BD) simulations to model the tethered diffusion of nanoparticles attached to proteins. We generate and analyze artificial images for various labeling strategies, nanoparticle sizes, and imaging parameters and test the fidelity of Gaussian PSF fitting in each scenario. We assess what systematic biases and artifacts may occur in the tracking of nanoparticle-labeled proteins and suggest best practices for designing and analyzing nanoparticle tracking experiments. Next, we simulate kinesin stepping to test for differences between real and observed outputs in similar scenarios. Surprisingly, we find that seeing is not always believing and that changes in the position and variance of nanometric tracking traces do not in all cases report the true dynamics of the labeled protein. To verify our predictions, we carry out kinesin nanoparticle tracking experiments and use simulations to interpret our data. We find that apparent differences between the two studies result from differences in the attachment position of the gold nanoparticle to the kinesin head and conclude that the studies are measuring the same underlying behavior.

MATERIALS AND METHODS

BD simulations

We used BD with a 1-ns time step to simulate the diffusional motion of overdamped spherical gold nanoparticles and the kinesin motor domain, which was modeled as a 5-nm diameter sphere. Particle dynamics were modeled using the overdamped Langevin equation, which describes the Brownian, viscous, and tether forces on the objects (35):

$$-\gamma \frac{d\vec{x}}{dt} + \sqrt{2D}\vec{f}_{therm} = \vec{F}_{spring}. \quad (1)$$

Here, $\gamma = 6\pi\eta r$ is the drag coefficient of a sphere with radius r diffusing in a medium with viscosity η equal to that of water, \vec{f}_{therm} represents a zero-mean Gaussian white noise process that describes the thermal fluctuations of the particle (36), and $(D = k_bT/\gamma)$ is Einstein's diffusion coefficient where k_bT is Boltzmann constant times absolute temperature. \vec{F}_{spring} represents the elastic properties of the tether, which are modeled as worm-like chain entropic springs (37,38).

$$\vec{F}_{spring} = \frac{k_bT}{4l_p} \left[\left(1 - \frac{x}{l_c} \right)^{-2} - \frac{1}{4} + \frac{x}{l_c} \right]. \quad (2)$$

Here, l_c is the contour length, l_p is the persistence length, and x is the end-to-end distance of the tether. Combining Eqs. 1 and 2 yields the following:

$$\frac{d\vec{x}}{dt} = \frac{1}{\gamma} \sqrt{2D}\vec{f}_{therm} - \frac{1}{\gamma} \frac{k_bT}{4l_p} \left[\left(1 - \frac{x}{l_c} \right)^{-2} - \frac{1}{4} + \frac{x}{l_c} \right]. \quad (3)$$

This first order stochastic differential equation was numerically integrated using a modified Euler method to obtain the dynamics of the free head, as follows (36):

$$\vec{x}_{n+1} = \vec{x}_n + \frac{1}{\gamma} \sqrt{2D\Delta t} \vec{f}_{therm} + \frac{1}{\gamma} \vec{F}_{spring} \Delta t. \quad (4)$$

Interaction forces were modeled using a hard wall potential, such that if the distance between two interacting objects was less than the sum of their radii, a collision was said to occur. To reconcile collisions, a modified event-driven collision detection and resolution algorithm was used (39,40). If a collision occurs, the minimal displacement is computed between the interjecting objects by assigning fictive velocities, \vec{v}_i , to the objects for the time step, Δt :

$$\vec{v}_i = \frac{\Delta \vec{x}_i}{\Delta t}. \quad (5)$$

The collision time, t_c , is determined by solving for the good root of the equation:

$$|\vec{d}_{ij} + \vec{v}_{ij}t_c| = \sigma_{ij}, \quad (6)$$

where the variable \vec{v}_{ij} is the relative velocity between the colliding objects, $\vec{v}_{ij} = \vec{v}_i - \vec{v}_j$. The collision is reconciled by mapping to the Brownian center of mass frame and reflecting the incident velocities along the normal vector between the objects and completing the remaining fraction of the time step with the new, postcollision velocities. The postcollision velocities are related to the precollision velocities, according to the diffusion coefficients of the objects, D_i and D_j , as follows (36):

$$\begin{bmatrix} \frac{D_j - D_i}{D_i + D_j} & \frac{2D_i}{D_i + D_j} \\ \frac{2D_j}{D_i + D_j} & \frac{D_i - D_j}{D_i + D_j} \end{bmatrix} \begin{bmatrix} v_i \\ v_j \end{bmatrix} = \begin{bmatrix} v'_i \\ v'_j \end{bmatrix}, \quad (7)$$

More explicitly, the postcollision positions of the interjecting objects are calculated as follows (36):

$$\vec{x}'_i = \vec{x}_i + \vec{v}_i t_c + \vec{v}'_i (\Delta t - t_c). \quad (8)$$

Artificial image generation

A stochastic photon emission process was used to generate artificial images, and the images were compiled into videos. The first step was to simulate the nanoparticle dynamics through the numerical integration of the Langevin equation of motion for 1 ms of simulated time. Once a vector of particle positions was obtained, the (x, y) coordinates were subsampled to the desired exposure window. The emission of photons from the diffusing nanoparticle was assumed to be a Poisson process characterized by a mean number of photons per 1-ns time step, determined such that the desired saturation for the frame was accomplished by the end of the exposure time window. The photons were then distributed to various positions on an artificial pixel grid according to a normal random variable with SD calculated with the full width half maximum (275 nm) corresponding to the PSF of the imaging apparatus. Once the photons were distributed to their positions, the photon counts were binned into a 30×30 pixel grid, with each pixel measuring 37.4 nm wide and the counts converted into a 16-bit image. We then added photon shot noise and empirically determined Gaussian noise with an SD of 4000 (out of 65,535). The noised images were then analyzed using FIESTA software (41) to extract fitted particle positions.

Constructs and protein preparation

Drosophila KHC truncated at amino acid 559 with an N-terminal AviTag was biotinylated and purified as reported previously (15). To prepare human constructs, a plasmid containing Cys-lite KIF5B (C7S/C65A/C168A/C174S/C294A/C330S/C421A) was obtained from Addgene (#24430)

(Watertown, MA). Cysteines were placed at position S55 or E215 using site-directed mutagenesis performed on demand by GenScript (Nanjing, China). The N-terminal tag construct was made by adding the CAG sequence to the N-terminus. All constructs had a C-terminal 6xHis tag. The plasmids were transformed into BL21 (DE3) bacteria (New England BioLabs, Ipswich, MA) for expression. Proteins were purified by affinity chromatography and desalting into phosphate buffer saline (pH 7.0) with 10 μ M ATP. Proteins were then mixed with maleimide-polyethylene glycol (PEG2)-biotin (21901BID; Thermo Fisher Scientific, Waltham, MA) with a two to tenfold molar excess of protein (to ensure low biotinylation) and incubated on ice for 30 min before quenching with ~71.5 mM β -mercaptoethanol and desalting into 25A200 (25 mM K-ACES, 2 mM Mg-Acetate, 2 mM K-EGTA, 0.1 K-EDTA, 1 mM β -mercaptoethanol, and 200 mM KCl (pH 6.9)) plus 10 μ M ATP. The biotinylation percentage was determined by dividing the biotin concentration (measured using the Pierce Fluorescence Biotin Quantitation Kit, 46610; Thermo Fisher Scientific) by the total protein concentration (measured at A₂₈₀). The biotinylation percentage was 11.2% for S55C, 7.0% for E215C, 8.4% for human N-terminal, and 20.0% for *Drosophila* N-terminal.

Single-molecule experiments

Kinesins tagged with gold nanoparticles were tracked using a custom-built total internal reflection dark field microscope, as previously described (21,29,42). Images were recorded using a Basler Ace acA640-750um complementary metal-oxide-semiconductor camera (1000 frames per second, 945 μ s exposure). Flow cells were prepared as previously described (42). All experiments were done in the following imaging solution: 0.5 mg/mL casein, 10 μ M taxol, 20 mM glucose, 20 μ g/mL glucose oxidase, 8 μ g/mL catalase, 0.2 mg/mL bovine serum albumin, 1:200 β -mercaptoethanol, and 2 mM MgATP in BRB80 (80 mM K-PIPES, 1 mM EGTA, and 1 mM MgCl₂ (pH 6.8)). Substoichiometrically biotinylated kinesin motors (8–20% biotinylation) were incubated with a 3- to 10-fold molar excess of 30-nm diameter streptavidin-coated gold nanoparticles (BBI Solutions, Crumlin, U.K.; ratio of biotin/gold) on ice for 20–30 min. The gold nanoparticles were then spun down at 20,000 $\times g$ for 4 min (to remove all nonbiotinylated motors) and resuspended in imaging solution at ~300 pM gold. Motor position over time was determined using FIESTA software (41). 2D step-size histograms were built by applying a modified version of the Tdetector step-finding algorithm (43) with 99.9% confidence intervals to the three-frame median-filtered Y axis (along microtubule axis) data. X axis (perpendicular to microtubule axis) step sizes were determined by calculating the difference in mean plateau values between change points detected by the algorithm along the Y axis.

RESULTS

Fidelity of the PSF fitting process falls if too few photons are collected in each exposure

To test how well the assumptions of PSF fitting hold for gold nanoparticle-labeled proteins, we developed a BD simulation regime for generating an artificial position versus time data for gold nanoparticles diffusing on a polypeptide tether (see Materials and Methods). We then generate artificial videos by stochastically emitting Gaussian-distributed photons from the nanoparticle center every 1 ns and bin the emitted photons into pixels to generate a grayscale image. Artificial images are then analyzed using FIESTA software (41), the same PSF fitting tool that we use to analyze our experimental nanoparticle

data. The particle positions fit by FIESTA are then compared to true particle position to test the fidelity of the PSF fitting process.

To address conditions under which positional information determined by PSF fitting becomes unreliable, we began by varying the photon count, analogous to altering the excitation intensity (13). We performed BD simulations of a tethered gold nanoparticle with a constant tether contour length (l_c), tether persistence length (l_p), and gold nanoparticle size (D_{gold}), varying only the number of photons per second collected from the gold. Artificial images were then generated, keeping a constant 600 μ s exposure time and 1000 frames per second frame rate, and the images were analyzed in FIESTA to extract fitted particle positions over time. To simulate our gold nanoparticle-labeled kinesin results, we modeled the tether as a worm-like chain with a 1 nm persistence length and 11.4 nm contour length, corresponding to kinesin N-terminal cover bundle plus

AviTag and the gold nanoparticle as a 30-nm diameter sphere (15,29,42,44). Example artificial images and corresponding nanometric tracking data for three different photon fluxes are shown in Fig. 1 B. To quantify the tracking fidelity, we calculated the SD of fitted particle positions for different photon fluxes. As expected, the relationship between photon count and tracking fidelity scaled as $1/N$ in the photon-limited regime in which background noise was significant and then transitioned to a $1/\sqrt{N}$ law at higher photon counts in which background noise became negligible (Fig. 1 B; (13)). Interestingly, the PSF fitting process continued to work optimally even at very high photon fluxes in which our artificial images became saturated. Indeed, a saturated center pixel slightly decreased the trace-wise SD (Fig. 1 B). Overall, these results recapitulated the well-known breakdown of the PSF fitting process at low photon counts (13), providing a quality check for our BD and image generation process.

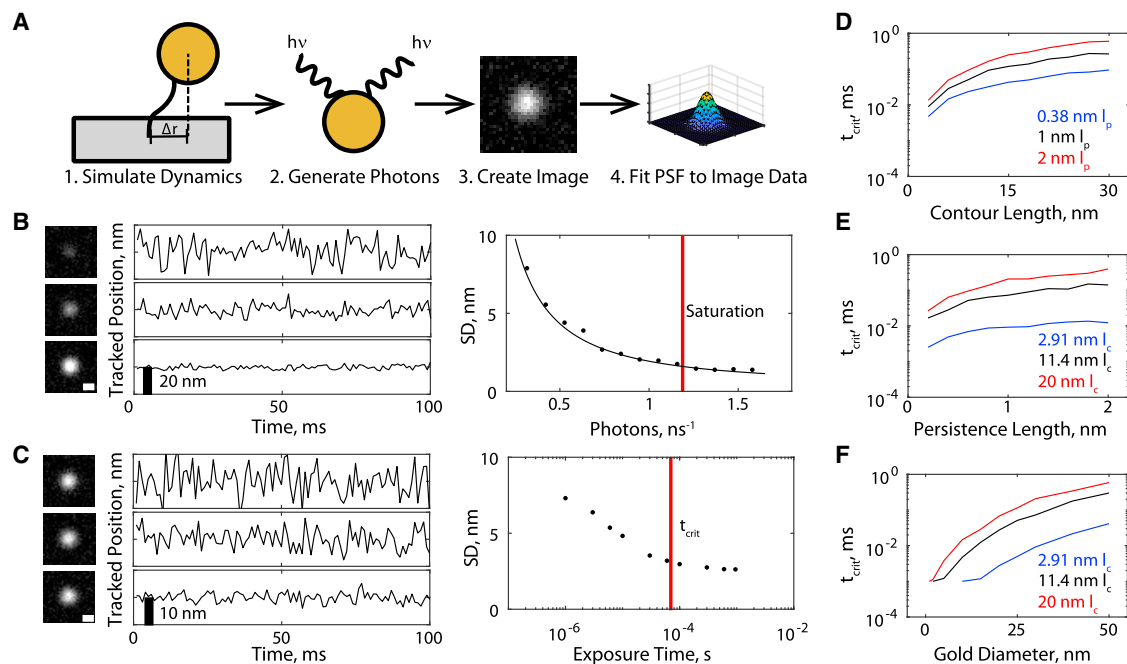


FIGURE 1 PSF fitting fidelity falls if too few photons are collected or if the exposure time is too small. (A) Shown is a diagram of simplified tethered gold diffusion system simulated with Brownian dynamics to create simulated images. The tether represents the conjugation system used to attach the gold nanoparticle to the protein of interest. BD simulations are run with a 1-ns time step, and photons are collected during a defined exposure time to generate an image frame that is then analyzed by PSF fitting. (B) Artificial images and PSF-fitted positions for BD simulations are run with $l_c = 12$ nm, $l_p = 1$ nm, $D_{Gold} = 30$ nm, $t_{expose} = 600 \mu s$, and $f = 1000$ frames per second. Only the number of photons emitted per second by the nanoparticle was changed between simulations. The three example images (top to bottom) show photon emission rates of 0.3, 0.6, and 1.5 photons per nanosecond, respectively. Black line shows fit to $\frac{a}{x} + \frac{b}{\sqrt{x}} + c$, where the first and second terms represent contributions of background noise and photon counting, respectively ($R^2 = 0.994$). Nanometric tracking fidelity was quantified as the SD of the position over the entire 100 ms trace. The vertical red line indicates where at least one pixel in the artificial images was saturated. (C) Artificial images and PSF-fitted positions for BD simulations are run with $l_c = 11.4$ nm, $l_p = 1$ nm, $D_{Gold} = 30$ nm, $f = 1000$ frames per second, and the photon flux is optimally set to nearly saturate the artificial images. Only the camera exposure time was changed between simulations. The three example traces (top to bottom) show exposure times of 1, 10, and 950 μs , respectively. The vertical red line indicates the critical exposure time, defined as the exposure time for which the SD was within 10% of its asymptotic value. Image scale bars in (B) and (C) represent 250 nm. (D) The critical exposure time is measured from simulated data for tethers with varying persistence lengths. All used a 30-nm nanoparticle. (E) The critical exposure time is measured from simulated data for tethers with varying contour lengths. All used a 30-nm nanoparticle. (F) The critical exposure time is measured from simulated data for tethered gold nanoparticles with varying diameters. All used a 1-nm persistence length. To see this figure in color, go online.

Fidelity of PSF fitting falls at low exposure times even when the photon count is very high

We next asked whether the PSF fitting process is able to work at arbitrarily high frame rates. To test this, we reran the BD simulations but, this time, varied the camera exposure time used to generate artificial images. We adjusted the photon generation rate such that the center pixel saturated for each image regardless of the exposure time (red line in Fig. 1 B, center panel), providing an optimal image. We tested a wide range of exposure times and found a robust trend that the SD of tracked particle positions increased at very short exposure times despite optimal photon collection (Fig. 1 C). In observing the dynamics of the tethered gold particle, we noted that the cause of this failure was undersampling—if the stationary distribution of nanoparticle tethered diffusion positions is not filled out in a given exposure, then the nanoparticle effectively becomes a time-varying point source, and tracking fidelity decreases (Fig. S1). To characterize this phenomenon, we identified the critical exposure time, t_{crit} , defined as the exposure time for which the SD of the fitted particle position rises above 10% of its baseline value (Fig. 1 C). The existence of this critical exposure time demonstrates that, independent of the number of photons collected, the PSF fitting process cannot be extended to arbitrarily high frame rates because the diffusion of the particle comes into play.

We next sought to identify the primary physical determinants of the critical exposure time for a generalized tethered particle system. To do this, we ran BD simulations using varying tether persistence lengths, tether contour lengths and gold nanoparticle diameters, and quantified the dependence of t_{crit} on these physical parameters (Fig. 1, D–F). We tested contour lengths from 2.91 nm, representing a short chemical tag, to 30 nm, longer than the length of an antibody tag. Similarly, we tested persistence lengths from 0.2 nm, approximating a lower bound of polymer tags, to 2 nm, approximating the persistence length of single-stranded DNA (45,46). We found that the contour length and nanoparticle diameter had the largest impacts because of their direct control over how rapidly the nanoparticle explores the tethered diffusion space; t_{crit} depended less strongly on the tether persistence length. These results point to the fact that smaller nanoparticles and tighter protein-nanoparticle conjugations are the best methods for enabling high-fidelity nanometric tracking at very high frame rates.

Short tethers lead to more collisions between protein and the attached nanoparticle

The results in Fig. 1 indicated that using the tightest possible conjugation method, particularly by reducing the tether contour length, allowed for higher experimental frame rates for single-molecule tracking. We wondered, however, if there

were any drawbacks to using such a tight tether. To investigate this question, we ran BD simulations on a double-tethered diffusion system, in which a protein of interest (modeled as a 5-nm diameter sphere) was tethered to the glass surface, and a 30-nm gold nanoparticle was tethered to the protein (Fig. 2 A). This system represents the tagging of a single protein domain that is attached to another domain via an unstructured region (for example, the one head-bound state of kinesin) (15). In this system, the nanoparticle can collide with the protein, in which case, the position of each was corrected assuming the conservation of energy and linear momentum (39,40) (see Materials and Methods). Thus, the attached particle is able to alter the position of the protein, which may introduce experimental artifacts. Examples of the stationary distributions of both the protein and the nanoparticle are shown in Fig. 2 B. As expected from

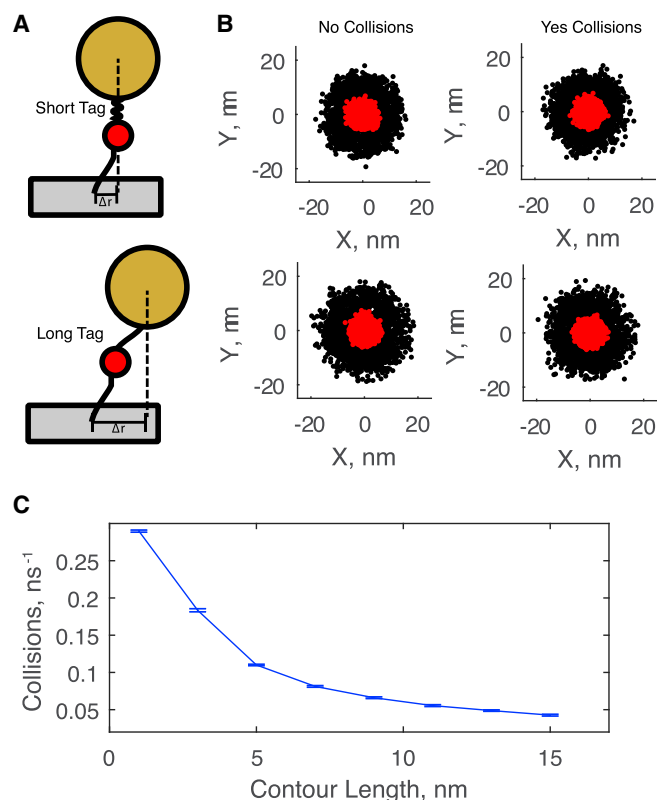


FIGURE 2 Tethers with shorter contour lengths lead to more frequent collisions between the gold nanoparticle and the tagged protein. (A) (Top) Shown is a diagram of the double-tethered diffusion system. The tether between the glass and the protein has a constant $l_p = 1$ nm and $l_c = 10.4$ nm. The tethers between the protein and the gold have $l_p = 1$ nm and $l_c = 2.91$ nm (short) or 11.4 nm (long). (B) Stationary distributions of both the protein (red) and the nanoparticle (black) for short (top) and long (bottom) tethers are generated in BD simulations. Collisions between the nanoparticle and the protein were allowed in the left column but not the right column. (C) The number of detected collisions between the nanoparticle and the protein as a function of tether contour length is shown. Error bars represent mean \pm SEM for $n = 30$ measurements. To see this figure in color, go online.

both the double tether and the larger radius of the particle, the distribution of particle positions is significantly broader than the distribution of protein positions. To test the influence of the protein-nanoparticle tether length, simulations were run for both a short tether (2.91 nm, corresponding to a biotin-PEG-maleimide linkage) and long tether (11.4 nm, corresponding to the 31 amino acids comprising the N-terminal cover strand and AviTag of kinesin-1) (15,47). As a baseline for comparison, we simulated a case in which collisions were not allowed, and the protein and nanoparticle were free to diffuse through each other. Allowing collisions did not significantly change the shape of the stationary distributions (Fig. 2 B), reinforcing that gold nanoparticle-labeling in general does not strongly perturb protein dynamics. To understand the nanoscale dynamics of the system, we also quantified the number of collisions between the particle and protein domain. Longer protein-nanoparticle tethers resulted in a collision roughly every 20 ns, but this rate increased steeply as the tether length was shortened (Fig. 2 C). Hence, although shorter tethers have the benefit of enabling higher frame rates to be used in gold nanoparticle tracking experiments, they have the drawback of leading to higher collision frequencies.

Changes in the rotational freedom of the gold-labeled protein can lead to apparent translations in fitted particle positions

We next investigated the effect of fixing the protein-nanoparticle tether position in the double-tethered diffusion model. Having the tether fixed to one side on the surface of the protein is akin to the protein lacking the ability to freely rotate. Hence, switching back and forth between a side-fixed and centered (freed) protein-nanoparticle tether position on the surface of the protein is akin to the protein losing and gaining rotational freedom. An example of this is a single nanoparticle-labeled motor domain in a progressively stepping kinesin dimer—when the motor domain binds to the microtubule, it is rotationally constrained, fixing the protein gold tether position with respect to time, whereas when the motor domain detaches and undergoes its own tethered diffusion, the tether position rotates along with it. To investigate this system, we ran BD simulations for a 5-nm protein tagged with a 40-nm nanoparticle and set the tether position either on top of the protein or fixed to one side (Fig. 3 A). For both cases, we used a contour length of 2.91 nm, a persistence length of 0.38 nm, a camera exposure time of 100 μ s, and a frame rate of 1000 frames per second. Example stationary distributions of protein and gold positions are shown in Fig. 3 B. When the tether was fixed to the right, we observed a systematic rightward bias in the gold position. We quantified the bias by running BD simulations, in which the system switched between freed and fixed tether position every 100 ms, and performing PSF

fitting analysis on the resulting artificial images. Example nanometric tracking data is shown in Fig. 3 C. Clear jumps in the X direction are seen for the tracked position despite the fact that the true protein position was constant over time. Hence, changes in the rotational freedom of a double-tethered diffusion system is sufficient to create apparent translations in the tracked position of nanoparticle-tagged proteins.

To investigate the physical determinants of the biased particle positions seen in Figs. 3 B and 4 C, we reran the BD simulations with tether point switching and varied the persistence and contour length of the protein gold tether and the nanoparticle diameter. We observed that changing the persistence length only weakly changed the magnitude of the apparent translation measured via PSF fitting when the system gained or lost rotational freedom (Fig. 3 D). In contrast, long contour length tethers strongly diminished rotation-driven artifactual translations observed via PSF fitting (Fig. 3 E). Reducing the gold diameter similarly diminished the apparent translation—shrinking the gold down below the size of a fluorescent protein nearly abolished artifactual translations (Fig. 3 F). Overall, these results emphasize that PSF fitting of gold-tagged proteins can produce apparent translations when the protein gold tether point rotates—displacements that can easily be misinterpreted as true movement of the protein. The best way to alleviate these artifacts is to use very small nanoparticles or to use tethers that are longer but still act as worm-like chains.

Different label positions lead to different apparent kinesin stepping patterns in experimental nanometric tracking data

We next experimentally explored the transition of the molecular motor kinesin from the two heads-bound state that completes a stepping cycle to the ATP waiting state that begins the next stepping cycle. A conflict has arisen in recent years as gold nanoparticle tracking data from different labs has yielded apparently different stepping patterns. Kinesin has long been shown to take 16.4-nm steps when one head is tracked (10), but with gold nanoparticle tracking, different substep patterns have become apparent (15,28). Tracking data from our own lab, in which we attached the gold nanoparticle at the N-terminus of one head, yielded a transition to the ATP waiting state that did not cause any apparent translation (15). Tracking data from the Tomishige Lab, in which the gold nanoparticle was attached at the back center of the head, yielded a transition to the ATP waiting state that was accompanied by an apparent forward and rightward translation (28). In an accompanying supporting figure of the article, traces in which the nanoparticle was attached at the front center of the head showed an apparent backward and rightward translation during the transition to the ATP waiting state (28). The authors suggested that a rotation of

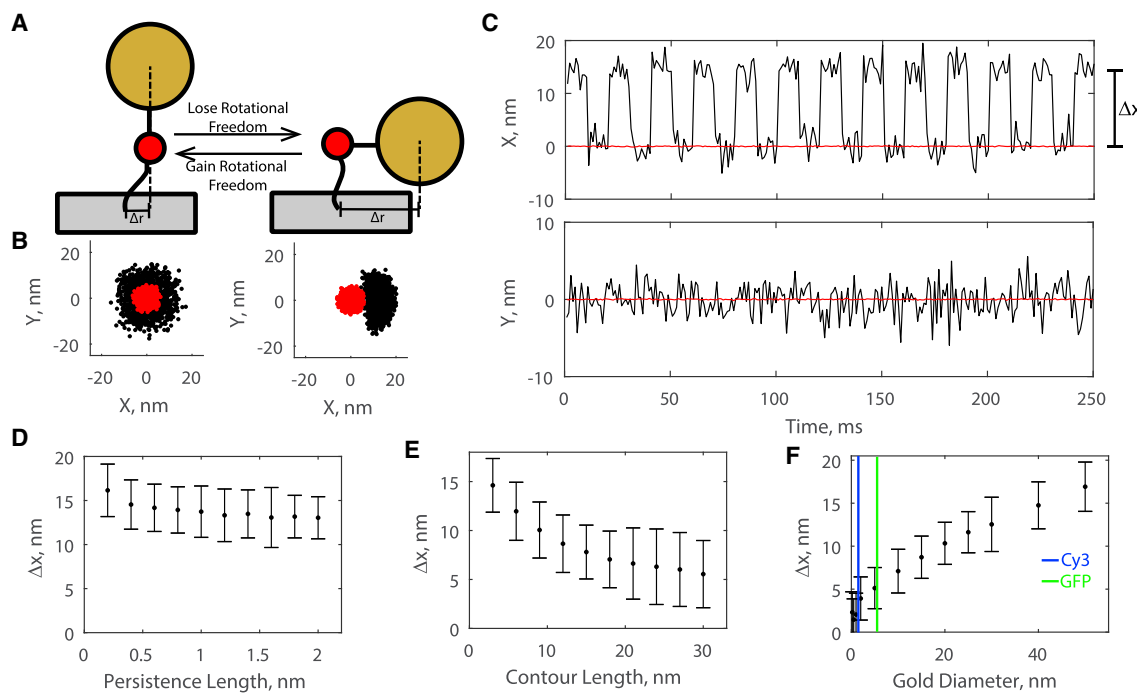


FIGURE 3 Changing rotational freedom can produce artifactual translations in nanometric tracking of gold nanoparticle-tagged proteins. (A) Shown is a double-tethered diffusion system, in which the rotational freedom of the tagged protein can be gained or lost by freeing or fixing the protein/gold tether connection point. (B) Stationary distributions of protein and gold nanoparticle positions are shown. Losing rotational freedom biased the position of the gold (black) to one side of the protein (red). Both BD simulations are run with $l_c = 2.91$ nm, $l_p = 0.38$ nm, $D_{\text{Gold}} = 40$ nm, $t_{\text{expose}} = 600 \mu\text{s}$, and $f = 1000$ frames per second. (C) Shown is the nanometric tracking data of a system that switches between high and low rotational freedom (matching B) every 10 ms. Clear artifactual translations of magnitude Δx occurred whenever the system switched. (D) Magnitude of the artifactual translation was tested at multiple persistence lengths, all with $l_c = 2.91$ nm, $D_{\text{Gold}} = 40$ nm, $t_{\text{expose}} = 600 \mu\text{s}$, and $f = 1000$ frames per second. Each point shown is mean \pm SD for $n = 100$ simulated switches. (E) Magnitude of the artifactual translation was tested at multiple contour lengths, all with $l_p = 0.38$ nm, $D_{\text{Gold}} = 40$ nm, $t_{\text{expose}} = 600 \mu\text{s}$, and $f = 1000$ frames per second. Each point shown is mean \pm SD for $n = 100$ simulated switches. (F) Magnitude of the artifactual translation was tested at multiple nanoparticle diameters, all with $l_c = 2.91$ nm, $l_p = 0.38$ nm, $t_{\text{expose}} = 600 \mu\text{s}$, and $f = 1000$ frames per second. Each point shown is mean \pm SD for $n = 100$ simulated switches. Diameters of an organic dye (Cy3) and green fluorescent protein (GFP) are shown for reference. To see this figure in color, go online.

the head caused these apparent translations, a point that our simulations (Fig. 3) quantitatively confirm as a possible explanation. We thus sought to clarify through experiments and simulations whether any translation of the rear head actually occurs during the transition to the ATP waiting state. A forward displacement to a state in which the tethered head is free to diffuse is predicted by models in which ATP binding causes a forward displacement of the tethered head via a ratchet type of mechanism in which neck linker docking involves passive diffusion and stabilization of the neck linker in a cleft (28,48). In contrast, if transition to the ATP waiting state involves no displacement of the tethered head, this implies that ATP binding causes a power stroke that physically removes the rear head from its previous binding site. Resolving this question is critical for defining the fundamental structural changes that underlie ATP-driven stepping of kinesin.

We tracked all three kinesin constructs previously used in our own and the Tomishige Lab's experiments with the same experimental setup, a custom-built TIRDFM (29,42,49). All

kinesin-tracking experiments were carried out under identical conditions— $10 \mu\text{M}$ ATP, BRB80 buffer, $22\text{--}23^\circ\text{C}$, 30-nm gold nanoparticles, bovine microtubules immobilized via rigor kinesin, casein surface blocking, and 1000 frames per second imaging with a $945 \mu\text{s}$ exposure time. The only difference was the kinesin construct used, with each having a different tether connection point. The S55 construct of human Cys-lite kinesin had the nanoparticle attached by a biotin-PEG-maleimide tether to the back center of the kinesin head (Fig. 4 A). The E215 construct of human Cys-lite kinesin had the nanoparticle attached by a biotin-PEG-maleimide tether to the front-center of the kinesin head (Fig. 4 B). Finally, the K560-AviN construct of *Drosophila melanogaster* kinesin had the nanoparticle attached via an N-terminal AviTag to the center right of the kinesin head (Fig. 4 C). As a control for the human versus fly kinesin, we also created an N-terminal, biotin-PEG-maleimide-labeled human Cys-lite construct (Fig. S2). Stepping data for the S55 construct (rear label) showed a rightward and forward displacement during the

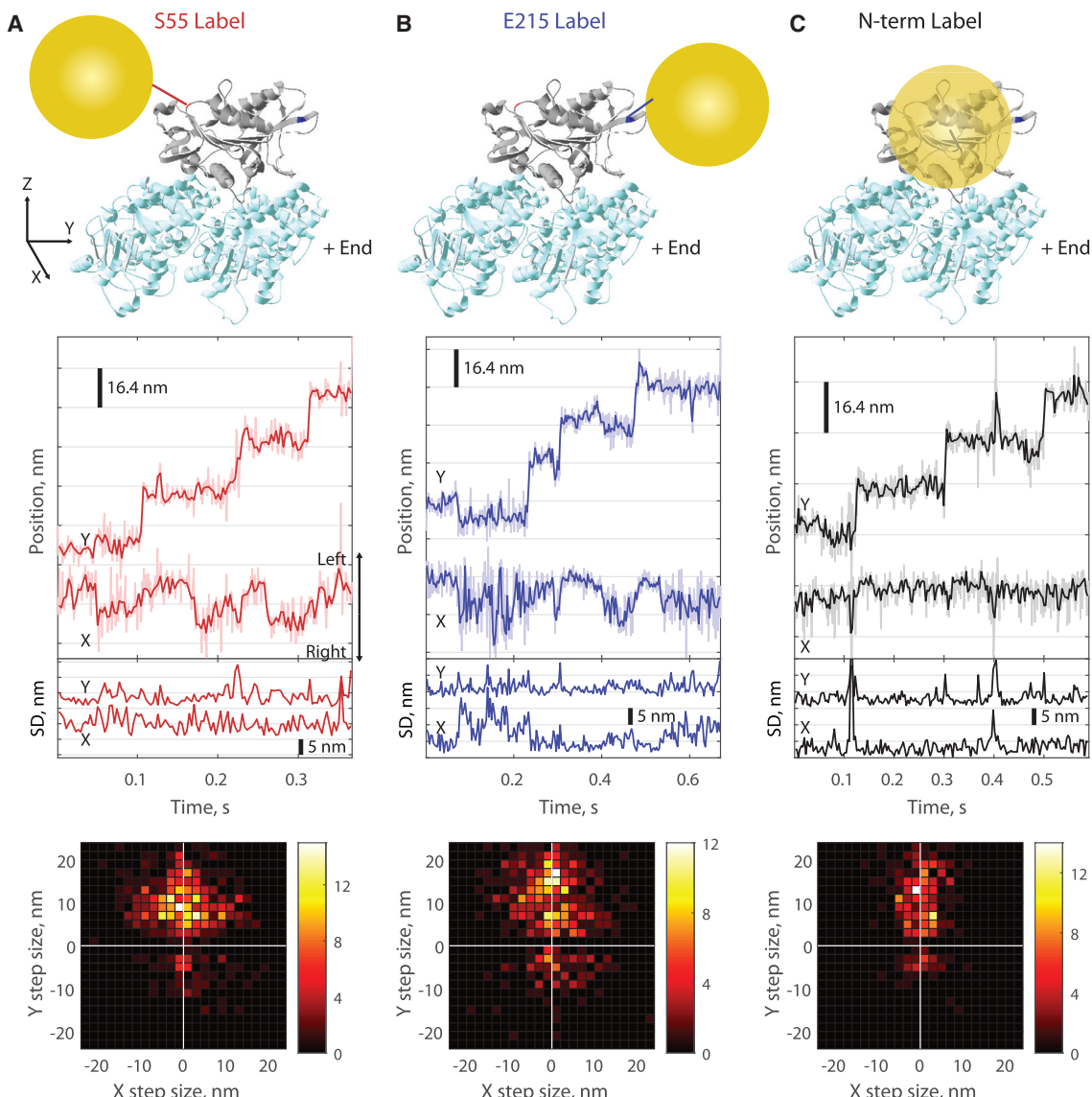


FIGURE 4 Experimental gold nanoparticle traces show that the apparent position of the ATP waiting state depends on the gold nanoparticle attachment position. (A) Shown is Cys-Lite with a cysteine introduced at S55, positioning the gold nanoparticle at the rear-enter of the kinesin head. Example traces and step size distributions ($n = 554$ steps from 18 traces) show a forward (along microtubule axis, Y) and rightward (perpendicular to microtubule, X) transition to the ATP waiting state, followed by a forward and leftward transition to the next binding site, summing to 16.4 nm along the microtubule. The 2D step-size distribution includes both transitions and thus shows a density at +8 nm in Y that is symmetric in X . (B) Shown is Cys-Lite with a cysteine introduced at E215, positioning the gold nanoparticle at the front center of the kinesin head. Example traces and step size distributions ($n = 469$ steps from 16 traces) show a backward and rightward transition to the ATP waiting state, followed by a forward and leftward transition to the next binding site. These transitions are seen as densities at negative Y , positive X and at positive Y , negative X . (C) Shown is *D. melanogaster* K560-AviN with a biotinylated N-terminus, positioning the gold at the right side of the kinesin head. Example traces and step size distributions ($n = 295$ steps from 17 traces) show no detectable transition to the ATP waiting state. The narrow 2D density distribution, which contrasts with the other constructs, shows that minimal movements perpendicular to the microtubule were detected. All dark colored traces are downsampled with a median or SD boxcar from 1000 to 333 frames per second. Sudden spikes in SD are sudden losses in tracking precision to free-diffusing gold nanoparticle overlapping with the walking kinesin. Shown is the crystal structure of human kinesin in the no-nucleotide state on microtubules (Protein Data Bank [PDB]: 3j8X) from Shang et al. (51). Gold not to scale. Additional example traces are shown in Fig. S2. To see this figure in color, go online.

transition to the ATP waiting state (Fig. 4 A; Fig. S2). Observing example traces and a 2D histogram of step sizes in the Y (along microtubule axis) and X (perpendicular to microtubule axis) directions, this transition appears as ~8 nm forward and ~5 nm rightward movement, followed

by an ~8 nm forward and ~5 nm leftward movement to complete a full ~16 nm step. Because the 2D histogram in Fig. 4 A includes all detected transitions, the distribution appears as a density at +8 nm that is laterally symmetric. Stepping data for the E215 construct (front label) showed

a rightward and backward displacement during the transition to the ATP waiting (Fig. 4 B; Fig. S2). This is seen in the 2D step size distributions as weight in positive *X* and negative *Y* that is not present for the other constructs. Finally, stepping data for the N-term (right side label) fly and human showed no displacement in any direction during the transition to the ATP waiting state (note the narrow step size distribution relative to the other constructs in the 2D distribution; Fig. 4 C; Fig. S2). Hence, these results replicated all existing experimental data on the same setup in the same conditions, isolating the tether position as the only possible cause for the differences in the apparent stepping patterns.

It should be noted that the motors are likely able to walk on different protofilaments, and because of the cylindrical geometry of the microtubule, different protofilaments will result in different observed lateral displacements. Our microscopy approach does not detect information in the *Z* direction; therefore, data are pooled without knowledge of whether the motors are walking along the top protofilament (which provides the largest signal from any lateral fluctuations) or a lateral protofilament (in which lateral motor fluctuations are reduced or are invisible to us). The scatter in the 2D position distributions is thus expected based on the geometry of the experiment.

Simulated kinesin traces show that the ATP waiting state is rotationally free but undisplaced longitudinally from the previous binding site

The experimental data shown in Fig. 4 may be explained by three different models for the ATP waiting state (Fig. 5 A) as follows: 1) In the unbound-displaced model, transition to the ATP waiting state results in the rear head moving forward into a true one head-bound state with rotational freedom; 2) in the unbound-undisplaced model, the rear head has rotational freedom but is not significantly translated from the rear binding site in the longitudinal direction; and 3) in the bound-undisplaced model, the rear head is fully attached to the rear binding site and thus rotationally constrained. To differentiate between these three models, we performed BD simulations of a labeled kinesin head, approximated as a 5-nm diameter sphere, bound to a microtubule, and modeled as a 25-nm cylinder. We ignored collisions of the labeled head with the second (unlabeled) head, as it led to complex collisional behavior not seen in experimental data (Fig. S3). Motors were stepped along the top-most protofilament. We tested kinesin with a 30-nm gold nanoparticle attached at the S55, E215, and N-terminal locations via a short tether with $l_c = 2.91$ nm and $l_p = 0.38$ nm, corresponding to the biotin-PEG-maleimide linker used in the experiments. The S55, E215, and N-terminal constructs were modeled by

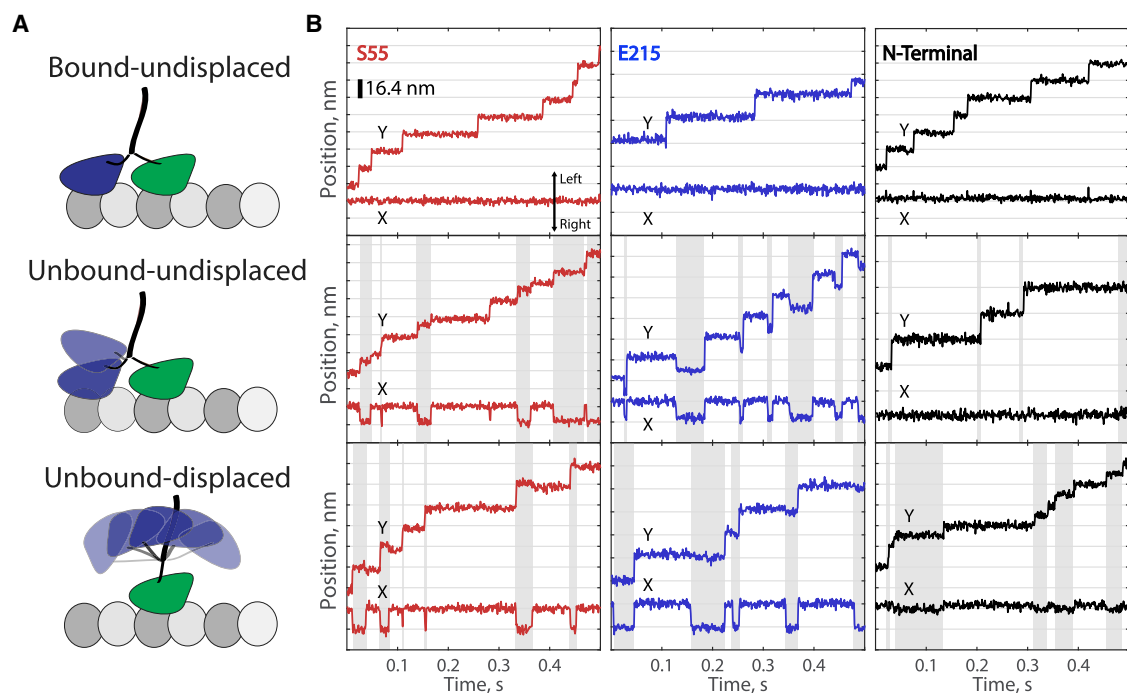


FIGURE 5 Simulated kinesin stepping best supports an unbound-undisplaced ATP waiting state. (A) Schematic shows the position of the tracked head in three different potential head configurations during the ATP waiting state. (B) Shown is the simulated tracking data for the S55, E215, and N-terminal labeling positions at low ATP and assuming the corresponding configuration for the ATP waiting state from (A). Gray shading indicates that the labeled head is unbound from the microtubule. Only the unbound-undisplaced model matched the experimental data for all three tag positions. To see this figure in color, go online.

positioning the tether attachment point at the rear, front, and right sides, respectively, of the unlabeled (bound) head.

Stepping was simulated by stochastically switching the gold-labeled kinesin head between a bound state in which it is rigidly attached to the microtubule and an unbound state in which it is tethered to the right-hand surface of the second, microtubule-bound head through their neck linker domains (modeled as a 28 amino acid polypeptide with $l_c = 10.4$ nm and $l_p = 1$ nm (36)). In the bound state, the kinesin gold tether point was fixed (at the front, back, or side of the bound head, depending on the construct), corresponding to the head having no rotational freedom. In the unbound state, the tether point on the unbound head was freed, corresponding to the head having full rotational freedom. To simulate a rotationally free state (without explicitly modeling the rotation of rigid bodies), the tether attachment point was assumed to lie on the minimal translational vector between the center of the nanoparticle and the center of the unbound head. We then simulated the three models for the ATP waiting state as follows. For the unbound-displaced model, the head was translated forward 8.2 nm and had complete rotational freedom. For the unbound-undisplaced model, the head was not translated along the microtubule but had complete rotational freedom. For the bound-undisplaced model, the head was not displaced and was rigidly attached. Because the ATP waiting state dominates the

hydrolysis cycle at 10 μ M ATP (15), we did not include the ATP-independent posthydrolysis state (15,28,42,50) in any of the three models. Completion of the step was modeled by translating the head forward either 8.2 or 16.4 nm to the next binding site and having it rigidly bind there. During all unbound states, we displaced the free kinesin head laterally to the right because the simulated traces did not replicate the experimental data otherwise (Fig. S4). The head was moved to a position equivalent to the adjacent protofilament of a 13 protofilament microtubule, 6.97 nm to the right and 0.78 nm down. This lateral translation is not unreasonable because the neck linker connecting the two heads emerges from the right side of the bound (unlabeled) head (see Discussion) (51).

In comparing the simulated stepping data in Fig. 5 B to the experimental stepping data in Fig. 4, only the unbound-undisplaced model agrees with the experiments (Fig. 6; Table 1). For the unbound-displaced model, the simulated S55 and E215 constructs showed little net movement along the microtubule axis during the ATP waiting state. The simulated N-terminal construct meanwhile clearly displayed the forward transition to the ATP waiting state—a feature never seen in the experimental data. For the bound-undisplaced model, both the simulated S55 and E215 constructs failed to show rightward motion, inconsistent with the experimental data. The unbound-undisplaced data

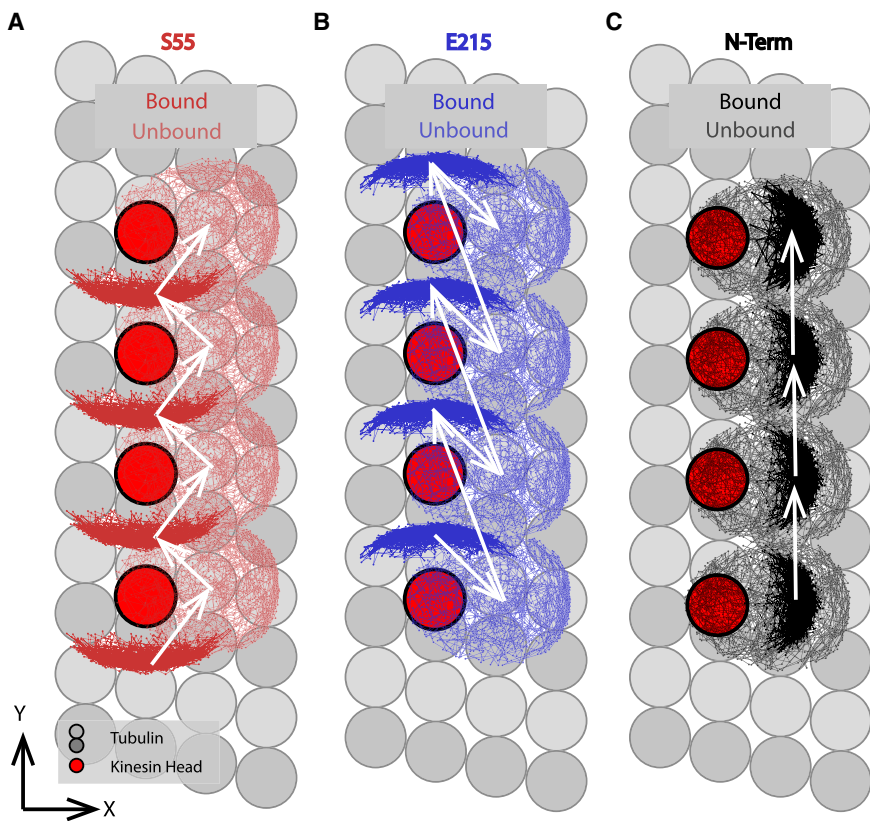


FIGURE 6 Characteristic stationary distribution of the nanoparticle during several steps of the model unbound-undisplaced kinesin stepping pattern. Red circles denote the successive locations of the labeled kinesin head when bound to the microtubule. White arrows denote translations of the nanoparticle stationary distribution. The (A) S55 labeling position (*rear of head*) shows a clear rearward bias in the 2HB state, with a transition forward and to the right as the head enters the ATP waiting state, whereas the (B) E215 labeling position (*front of head*) shows a clear forward bias in the 2HB state, with a transition backward and to the right as the head enters the ATP waiting state. (C) The N-term labeling position (*right side of head*) has a rightward bias throughout the step of the kinesin. The rightward transitions of the labeled head are counteracted by the inherent rightward bias of the N-term label in the 2HB state. Each data point represents 1 μ s. To see this figure in color, go online.

TABLE 1 Summary of the Apparent Position of the Rear Head in the ATP Waiting State for Multiple Tagging Strategies

	S55 (Back)		E215 (Front)		N-term (Right Side)	
	Y	X	Y	X	Y	X
Experimental	Forward	Right	Backward	Right	None	None
Bound-undisplaced	None	None	None	None	None	None
Unbound-undisplaced	Forward	Right	Backward	Right	None	None
Unbound-displaced	Forward	Right	None	Right	Forward	None

Only the unbound-undisplaced simulated data matched the experimental data.

perfectly replicated all the key features observed in the experimental data: simulated S55 moved forward and rightward during the transition to the ATP waiting state, E215 moved backward and rightward, and N-terminal showed no displacement. Hence, the kinesin ATP waiting state is best described as being unbound and undisplaced, and the apparent differences in experimental tracking data (Fig. 4) can all be explained by differences in the labeling position.

DISCUSSION

In this study, we used BD simulations to explore the abilities and limitations of high-resolution nanometric tracking of proteins with gold nanoparticle labels. We found that the contour length of the protein-nanoparticle tether, the nanoparticle size, and the camera exposure time all strongly influence PSF fitting fidelity. We further showed that changes in the rotational freedom of gold nanoparticle-labeled proteins can lead to apparent translations in nanometric tracking data, even when the protein itself has not moved. Finally, we explored a standing dispute in the kinesin field and found that all reported experimental results are correct and that differences between reports in the literature are simply due to differences in the protein-gold tether position.

Advantages and disadvantages of single-molecule tracking with increasingly faster frame rates

Optimal nanometric tracking of a tagged protein inherently relies on two key assumptions. The first assumption is that the probe emits a sufficient number of photons during a given exposure time to overcome the $1/\sqrt{N}$ (N = photon number) proportionality of the image localization error. The second assumption is that the probe is a positionally constant point source of radiation. If either of these assumptions do not hold, then PSF fitting yields noisy positional data. Gold nanoparticle tracking circumvents the temporal limitation of traditional fluorophores by relying on light scattering, but the relatively slow particle diffusion may lead to noisy data if the exposure time is too short (Fig. 1 C). It is therefore prudent to carefully choose the exposure time used for every particular gold nanoparticle tracking experiment. Choosing the smallest possible exposure time

and, hence, the fastest possible frame rate will always yield the most possible information, particularly because tracking data can be averaged in postprocessing to obtain cleaner traces. However, if an exposure time shorter than the critical exposure time (Fig. 1 C) is used, then the new information gained will be about the dynamics of the gold and the tether not about the dynamics of the protein itself. This information may be of interest in certain cases in which the physical nature of the tether is of biological interest (for instance, in tethered particle motion) (52). However, for single-molecule tracking experiments in which the gold is meant to be a reporter of protein position, no new useful information about the protein is obtained in most cases. Also, very high frame rates often necessitate smaller fields of view and shorter total video durations. Hence, imaging a tagged protein beyond the critical exposure time may offer diminishing returns when trying to characterize the positional dynamics of the protein itself. The data provided here in Fig. 1, D–F serve as a good starting point for determining the critical exposure time for a given experimental system.

Observed positional changes in nanometric tracking data do not always correspond to true positional changes of the labeled protein

Unlike fluorescent dyes, which at several angstroms are substantially smaller than the proteins they label, gold nanoparticle probes are substantially larger than the proteins they are labeling. The small size of fluorescent probes means that the PSF of the probe is an accurate reporter of the protein position, whereas the large dimensions of gold nanoparticles opens the possibility that the position reported for the nanoparticle is not an accurate reflection of the protein position. Therefore, in interpreting image data, it is crucial to consider the effects that the large particle diameter have on any observed displacements. For many processive enzymes, the major mechanochemical states in their cycles consist of transitions from a highly constrained, ordered (bound) state to a more disordered (unbound) one (2,15). When the protein is in an ordered state, the tether attachment point and geometry play key roles in determining the search space of the gold nanoparticle, especially when the tether has a shorter contour length, or the gold nanoparticle is large. These effects can lead to a systematic bias in the gold nanoparticle position relative to the protein position

(Fig. 3). If the protein itself gains or loses rotational freedom, then this systematic bias can be transferred from the Z positional distributions, which PSF fitting is blind to, to the XY positional distributions, which PSF fitting can directly detect. Hence, if a protein switches its conformational state and undergoes any type of rotational change, PSF fitting will report a positional change of a magnitude related to the probe size and tether contour length, even if the protein itself does not move (Fig. 3). This phenomenon has been observed directly in gold nanoparticle tracking of myosin (30), and the effects of rotational relaxation have similarly been seen in trapping studies, in which the probes are a further order of magnitude larger (53). The important point is that with gold nanoparticle tracking, seeing is not always believing; apparent abrupt changes in position over time data are certainly indicative of the labeled protein changing its conformational state, but they do not necessarily mean that the protein itself has changed position. In light of this phenomenon, different nanoparticle attachment positions and strategies on the same protein can lead to completely different nanometric tracking data.

The rear head of kinesin does not move forward upon transitioning to the ATP waiting state

Our experimental and simulated data show that the ATP waiting state of kinesin-1 is best described as a loose two heads-bound state in which the read head is unbound but undisplaced. Upon transition to the ATP waiting state, the rear head gains rotational freedom, and because the particle radius is six times the protein radius, these rotations can lead to large apparent translations (Figs. 4 and 5). For the S55 and E215 constructs, the tether position is along the microtubule axis, hence causing the artifactual translation to appear in the direction of stepping (Figs. 4 and 5). Thus, both of these constructs are unreliable reporters of the true head position along the microtubule axis when a large (30-nm) gold nanoparticle is used. The E215 construct has previously been used in nanometric tracking experiments with small fluorescent probes, and no translations were observed upon transition to the ATP waiting state (10,54,55). This is fully consistent with our claim of an unbound-undisplaced ATP waiting state because smaller probes have diminished artifactual translations due to rotation (Fig. 3 F) but still accurately report true translations of the tagged protein. These constructs do accurately report positions perpendicular to the microtubule, however, with the rightward movements of the head leading to the conclusion that the head is at least partially unbound. In contrast, N-terminal tagged kinesins have the tether attached to the right side of the head, meaning that artifactual translations caused by rotation only occur in the direction perpendicular to the microtubule. As such, these constructs are accurate reporters of protein position along the microtubule axis, regardless of probe size. We hence remain confident in

our previous claims that the posthydrolysis one head-bound intermediate is forward displaced by 8 nm and that the ATP waiting state can transition to a true unbound-displaced one head-bound state at longer timescales (15). These unbound-displaced states, not examined in the current study, are critical for determining kinesin processivity (42) and side-stepping probability (44,56). The unbound-undisplaced ATP waiting state suggested from our results is consistent with previous molecular dynamics studies, which show that the trailing head can hover near its previous binding site before neck-linker docking in the front head (57,58). An important implication of this ATP waiting state is that ATP binding in the front head drives complete detachment of the rear head, consistent with a mechanically gated power stroke-like stepping mechanism at physiological ATP (59,60) and with the necessity of a backward-oriented neck linker for interhead coordination (61,62).

The idea that the tethered head is free in the ATP waiting state originated from nucleotide half-site experiments by Hackney (63), who found that, upon collision with a microtubule, a dimeric kinesin loses only one of its two bound ADP molecules. This property argues for a state in which one head is bound to the microtubule, and the other is tethered and unable to interact with adjacent tubulin subunits. However, it should be remembered that this initial collision complex is an entry point into the normal ATP hydrolysis cycle that is not necessarily visited during normal stepping in saturating ATP. One question that was not fully answered from this tethered head model was, if the two neck linkers are disordered polypeptides, what prevents the tethered head from interacting with one of its adjacent tubulin sites? This question was clarified for the trailing binding site from the finding that docking of the neck linker, which would likely be necessary for the trailing head to attach to the rear tubulin, traps the bound nucleotide and hence would not trigger ADP release (64).

There is structural support in the literature for the ATP waiting state involving the trailing head remaining behind the bound head, near its previous binding site. In the original Rice et al. article that laid out the neck linker docking paradigm for kinesin-1, cryo-electron microscopy (cryoEM) images under no nucleotide conditions show neck linker positions in both a forward position and a backward right position (48). In more recent cryoEM structures of kinesin-1 and kinesin-3 in no nucleotide, the proximal segment of the neck linker is pointed rearward, although the distal portion of the neck linker is disordered (65). In agreement with an undisplaced rotationally free trailing head in kinesin-1, single-molecule Förster resonance energy transfer suggested a trailing orientation of the neck linker in the ATP waiting state (66), and single-molecule fluorescence polarization microscopy found that the tethered head was rotationally disordered in the ATP waiting state (67). There is strong evidence for a backward and rightward neck linker orientation in other kinesin families as well. For kinesin-5

under no nucleotide conditions, a backward facing neck linker has been seen in both x-ray crystallography of isolated heads (68,69) and cryoEM of microtubule-bound motors in the apo state (70). And in the kinesin-6, Zen-4, specific residues in the neck linker initial segment were shown to form a backward-oriented β strand with conserved sequences in the catalytic core; furthermore, swapping this short sequence into kinesin-1 resulted in an increase in the kinesin-1 run length (71). Thus, there is a preponderance of evidence that in the ATP waiting state, the tethered head is not freely diffusing centered on the bound head but instead is constrained to remain in its trailing position by the neck linker of the bound state (leading) head.

The kinesin head swings to the right during stepping

In our previous work using *D. melanogaster* K560 with an N-terminal AviTag, we did not observe a consistent rightward bias during stepping (15). This contrasted work from the Tomishige Lab, which reported substantial rightward movements for both the S55C and E215C constructs (28). Here, we experimentally replicated all three of these results (Fig. 4). BD simulations showed that these apparent stepping patterns can be explained by differences in the tether attachment position (Fig. 5). Because S55C and E215C have the gold nanoparticle on the front and rear, respectively, they are both capable of accurately reporting translations of the kinesin head perpendicular to the microtubule. The N-terminal construct, however, has its tether on the right side of the head. Hence, when kinesin transitions to the ATP waiting state, the head simultaneously gains rotational freedom (leading to a leftward translation of the gold) and is itself displaced rightward (leading to a rightward translation of the gold). These two translations cancel out, leading to no apparent rightward motion of the gold. We conclude that, just as the S55C and E215C constructs are unreliable reporters of head position along the microtubule axis, the N-terminal construct is an unreliable reporter of head position perpendicular to the microtubule axis. Rightward motion of the head during each step is consistent with recent measurements of torque being generated by kinesin held in an optical trap (72). Overall, both our work and the Tomishige Lab work are fully correct, and the apparent differences were merely due to tether position and nomenclature.

Gold nanoparticle tracking experiments utilizing PSF fitting have led to numerous advancements in understanding how molecular motors such as kinesin (15,20,28,29,33,42,49,73), myosin (30,31,34), dynein (26), the bacterial flagellar motor (18), and F1-ATPase (17,19) function. However, the fast frames rates and relatively large gold nanoparticle sizes introduce new caveats to the PSF fitting process which to date have not been wholly appreciated. We emphasize here that PSF fitting only works opti-

mally if the tethered nanoparticle has sufficient time to explore its entire stationary distribution of positions, meaning that gold nanoparticle tracking cannot practically be done at arbitrarily high frames rates even if a sufficient number of photons are collected per exposure. We further emphasize that conformational changes in proteins may lead to rotations in the protein-nanoparticle tether connection point, causing apparent translations in nanometric tracking data, despite the fact that no translation of the protein actually occurs. These lessons were used to immediately clarify a standing debate in the kinesin field and will continue to be valuable to biophysicists using gold nanoparticle tracking to investigate protein conformational dynamics.

SUPPORTING MATERIAL

Supporting Material can be found online at <https://doi.org/10.1016/j.bpj.2019.06.010>.

AUTHOR CONTRIBUTIONS

W.O.H., K.J.M., and J.F. designed the research. A.S.I.C. and J.P.J. developed and carried out simulations. K.J.M. carried out single-molecule experiments. K.J.M. and A.S.I.C. analyzed data. K.J.M. and W.O.H. wrote the initial draft, and all authors edited the manuscript.

ACKNOWLEDGMENTS

We are grateful to David Arginteanu for his help with protein preparation. This work was funded by National Institutes of Health R01GM076476 to W.O.H., R01GM122082 to W.O.H. and J.F., and a National Cancer Institute fellowship F99CA223018 to K.J.M. A.S.I.C. and J.P.J. were supported by American Heart Association 18UFEEL33900164.

REFERENCES

1. Selvin, P. R., and T. Ha. 2008. Single-Molecule Techniques: A Laboratory Manual. Cold Spring Harbor Laboratory Press, New York.
2. Shashkova, S., and M. C. Leake. 2017. Single-molecule fluorescence microscopy review: shedding new light on old problems. *Biosci. Rep.* 37:BSR20170031.
3. Betzig, E., and R. J. Chichester. 1993. Single molecules observed by near-field scanning optical microscopy. *Science*. 262:1422–1425.
4. Anderson, C. M., G. N. Georgiou, ..., R. J. Cherry. 1992. Tracking of cell surface receptors by fluorescence digital imaging microscopy using a charge-coupled device camera. Low-density lipoprotein and influenza virus receptor mobility at 4 degrees. *C. J. Cell Sci.* 101:415–425.
5. Schütz, G. J., H. Schindler, and T. Schmidt. 1997. Single-molecule microscopy on model membranes reveals anomalous diffusion. *Biophys. J.* 73:1073–1080.
6. Cheezum, M. K., W. F. Walker, and W. H. Guilford. 2001. Quantitative comparison of algorithms for tracking single fluorescent particles. *Biophys. J.* 81:2378–2388.
7. Bobroff, N. 1986. Position measurement with a resolution and noise-limited instrument. *Rev. Sci. Instrum.* 57:1152–1157.
8. Moerner, W. E., and L. Kador. 1989. Optical detection and spectroscopy of single molecules in a solid. *Phys. Rev. Lett.* 62:2535–2538.

9. Yildiz, A., J. N. Forkey, ..., P. R. Selvin. 2003. Myosin V walks hand-over-hand: single fluorophore imaging with 1.5-nm localization. *Science*. 300:2061–2065.
10. Yildiz, A., M. Tomishige, ..., P. R. Selvin. 2004. Kinesin walks hand-over-hand. *Science*. 303:676–678.
11. Yildiz, A., and P. R. Selvin. 2005. Fluorescence imaging with one nanometer accuracy: application to molecular motors. *Acc. Chem. Res.* 38:574–582.
12. Kural, C., H. Balci, and P. R. Selvin. 2005. Molecular motors one at a time: FIONA to the rescue. *J. Phys. Condens. Matter*. 17:S3979–S3995.
13. Thompson, R. E., D. R. Larson, and W. W. Webb. 2002. Precise nanometer localization analysis for individual fluorescent probes. *Biophys. J.* 82:2775–2783.
14. Svoboda, K., and S. M. Block. 1994. Force and velocity measured for single kinesin molecules. *Cell*. 77:773–784.
15. Mickolajczyk, K. J., N. C. Deffenbaugh, ..., W. O. Hancock. 2015. Kinetics of nucleotide-dependent structural transitions in the kinesin-1 hydrolysis cycle. *Proc. Natl. Acad. Sci. USA*. 112:E7186–E7193.
16. Soppina, V., S. R. Norris, ..., K. J. Verhey. 2014. Dimerization of mammalian kinesin-3 motors results in superprocessive motion. *Proc. Natl. Acad. Sci. USA*. 111:5562–5567.
17. Yasuda, R., H. Noji, ..., H. Itoh. 2001. Resolution of distinct rotational substeps by submillisecond kinetic analysis of F1-ATPase. *Nature*. 410:898–904.
18. Sowa, Y., B. C. Steel, and R. M. Berry. 2010. A simple backscattering microscope for fast tracking of biological molecules. *Rev. Sci. Instrum.* 81:113704.
19. Ueno, H., S. Nishikawa, ..., H. Noji. 2010. Simple dark-field microscopy with nanometer spatial precision and microsecond temporal resolution. *Biophys. J.* 98:2014–2023.
20. Schneider, R., T. Glaser, ..., S. Diez. 2013. Using a quartz paraboloid for versatile wide-field TIR microscopy with sub-nanometer localization accuracy. *Opt. Express*. 21:3523–3539.
21. Mickolajczyk, K. J., and W. O. Hancock. 2018. High-Resolution Single-Molecule Kinesin Assays at kHz Frame Rates. In *Molecular Motors. Methods in Molecular Biology*, 1805. C. Lavelle, ed. Humana Press, New York, NY, pp. 123–138.
22. Ando, J., A. Nakamura, ..., R. Iino. 2018. Single-nanoparticle tracking with angstrom localization precision and microsecond time resolution. *Biophys. J.* 115:2413–2427.
23. Lindfors, K., T. Kalkbrenner, ..., V. Sandoghdar. 2004. Detection and spectroscopy of gold nanoparticles using supercontinuum white light confocal microscopy. *Phys. Rev. Lett.* 93:037401.
24. Kukura, P., H. Ewers, ..., V. Sandoghdar. 2009. High-speed nanoscopic tracking of the position and orientation of a single virus. *Nat. Methods*. 6:923–927.
25. Ortega-Arroyo, J., and P. Kukura. 2012. Interferometric scattering microscopy (iSCAT): new frontiers in ultrafast and ultrasensitive optical microscopy. *Phys. Chem. Chem. Phys.* 14:15625–15636.
26. Andrecka, J., Y. Takagi, ..., P. Kukura. 2016. Interferometric scattering microscopy for the study of molecular motors. *Methods in Enzymol.* 581:517–539.
27. Lin, Y. H., W. L. Chang, and C. L. Hsieh. 2014. Shot-noise limited localization of single 20 nm gold particles with nanometer spatial precision within microseconds. *Opt. Express*. 22:9159–9170.
28. Isojima, H., R. Iino, ..., M. Tomishige. 2016. Direct observation of intermediate states during the stepping motion of kinesin-1. *Nat. Chem. Biol.* 12:290–297.
29. Chen, G. Y., K. J. Mickolajczyk, and W. O. Hancock. 2016. The kinesin-5 chemomechanical cycle is dominated by a two-heads-bound state. *J. Biol. Chem.* 291:20283–20294.
30. Andrecka, J., J. Ortega Arroyo, ..., P. Kukura. 2015. Structural dynamics of myosin 5 during processive motion revealed by interferometric scattering microscopy. *eLife*. 4:e05413.
31. Dunn, A. R., P. Chuan, ..., J. A. Spudich. 2010. Contribution of the myosin VI tail domain to processive stepping and intramolecular tension sensing. *Proc. Natl. Acad. Sci. USA*. 107:7746–7750.
32. Lebel, P., A. Basu, ..., Z. Bryant. 2014. Gold rotor bead tracking for high-speed measurements of DNA twist, torque and extension. *Nat. Methods*. 11:456–462.
33. Schneider, R., T. Korten, ..., S. Diez. 2015. Kinesin-1 motors can circumvent permanent roadblocks by side-shifting to neighboring protofilaments. *Biophys. J.* 108:2249–2257.
34. Dunn, A. R., and J. A. Spudich. 2007. Dynamics of the unbound head during myosin V processive translocation. *Nat. Struct. Mol. Biol.* 14:246–248.
35. Howard, J. 2001. Mechanics of Motor Proteins and the Cytoskeleton, Second Edition. Sinauer Associates, Sunderland, MA.
36. Kutys, M. L., J. Fricks, and W. O. Hancock. 2010. Monte Carlo analysis of neck linker extension in kinesin molecular motors. *PLoS Comput. Biol.* 6:e1000980.
37. Hariharan, V., and W. O. Hancock. 2009. Insights into the mechanical properties of the Kinesin neck linker domain from sequence analysis and molecular dynamics simulations. *Cell Mol. Bioeng.* 2:177–189.
38. Kellermayer, M. S., S. B. Smith, ..., C. Bustamante. 1997. Folding-unfolding transitions in single titin molecules characterized with laser tweezers. *Science*. 276:1112–1116.
39. Strating, P. 1999. Brownian dynamics simulation of a hard-sphere suspension. *Phys. Rev. E*. 59:2175–2187.
40. Scala, A. 2013. Brownian dynamics simulation of polydisperse hard spheres. *Eur. Phys. J. Spec. Top.* 216:21–29.
41. Ruhnow, F., D. Zwicker, and S. Diez. 2011. Tracking single particles and elongated filaments with nanometer precision. *Biophys. J.* 100:2820–2828.
42. Mickolajczyk, K. J., and W. O. Hancock. 2017. Kinesin processivity is determined by a kinetic race from a vulnerable one-head-bound state. *Biophys. J.* 112:2615–2623.
43. Chen, Y., N. C. Deffenbaugh, ..., W. O. Hancock. 2014. Molecular counting by photobleaching in protein complexes with many subunits: best practices and application to the cellulose synthesis complex. *Mol. Biol. Cell*. 25:3630–3642.
44. Hoeprich, G. J., K. J. Mickolajczyk, ..., C. L. Berger. 2017. The axonal transport motor kinesin-2 navigates microtubule obstacles via protofilament switching. *Traffic*. 18:304–314.
45. Lee, H., R. M. Venable, ..., R. W. Pastor. 2008. Molecular dynamics studies of polyethylene oxide and polyethylene glycol: hydrodynamic radius and shape anisotropy. *Biophys. J.* 95:1590–1599.
46. Murphy, M. C., I. Rasnik, ..., T. Ha. 2004. Probing single-stranded DNA conformational flexibility using fluorescence spectroscopy. *Biophys. J.* 86:2530–2537.
47. Hwang, W., M. J. Lang, and M. Karplus. 2008. Force generation in kinesin hinges on cover-neck bundle formation. *Structure*. 16:62–71.
48. Rice, S., A. W. Lin, ..., R. D. Vale. 1999. A structural change in the kinesin motor protein that drives motility. *Nature*. 402:778–784.
49. Feng, Q., K. J. Mickolajczyk, ..., W. O. Hancock. 2018. Motor reattachment kinetics play a dominant role in multimotor-driven cargo transport. *Biophys. J.* 114:400–409.
50. Verbrugge, S., Z. Lansky, and E. J. Peterman. 2009. Kinesin's step dissected with single-motor FRET. *Proc. Natl. Acad. Sci. USA*. 106:17741–17746.
51. Shang, Z., K. Zhou, ..., C. V. Sindelar. 2014. High-resolution structures of kinesin on microtubules provide a basis for nucleotide-gated force-generation. *eLife*. 3:e04686.
52. Schafer, D. A., J. Gelles, ..., R. Landick. 1991. Transcription by single molecules of RNA polymerase observed by light microscopy. *Nature*. 352:444–448.
53. Bugiel, M., E. Böhl, and E. Schäffer. 2015. The Kinesin-8 Kip3 switches protofilaments in a sideward random walk asymmetrically biased by force. *Biophys. J.* 108:2019–2027.

54. Toprak, E., A. Yildiz, ..., P. R. Selvin. 2009. Why kinesin is so processive. *Proc. Natl. Acad. Sci. USA.* 106:12717–12722.
55. Yildiz, A., M. Tomishige, ..., R. D. Vale. 2008. Intramolecular strain coordinates kinesin stepping behavior along microtubules. *Cell.* 134:1030–1041.
56. Mitra, A., F. Ruhnow, ..., S. Diez. 2018. Directionally biased sidestepping of Kip3/kinesin-8 is regulated by ATP waiting time and motor-microtubule interaction strength. *Proc. Natl. Acad. Sci. USA.* 115:E7950–E7959.
57. Zhang, Z., and D. Thirumalai. 2012. Dissecting the kinematics of the kinesin step. *Structure.* 20:628–640.
58. Zhang, Z., Y. Goldtzvik, and D. Thirumalai. 2017. Parsing the roles of neck-linker docking and tethered head diffusion in the stepping dynamics of kinesin. *Proc. Natl. Acad. Sci. USA.* 114:E9838–E9845.
59. Hancock, W. O. 2016. The kinesin-1 chemomechanical cycle: stepping toward a consensus. *Biophys. J.* 110:1216–1225.
60. Clancy, B. E., W. M. Behnke-Parks, ..., S. M. Block. 2011. A universal pathway for kinesin stepping. *Nat. Struct. Mol. Biol.* 18:1020–1027.
61. Andreasson, J. O., B. Milic, ..., S. M. Block. 2015. Examining kinesin processivity within a general gating framework. *eLife.* 4:e07403.
62. Dogan, M. Y., S. Can, ..., A. Yildiz. 2015. Kinesin's front head is gated by the backward orientation of its neck linker. *Cell Rep.* 10:1967–1973.
63. Hackney, D. D. 1994. Evidence for alternating head catalysis by kinesin during microtubule-stimulated ATP hydrolysis. *Proc. Natl. Acad. Sci. USA.* 91:6865–6869.
64. Kaan, H. Y., D. D. Hackney, and F. Kozielski. 2011. The structure of the kinesin-1 motor-tail complex reveals the mechanism of autoinhibition. *Science.* 333:883–885.
65. Atherton, J., I. Farabella, ..., C. A. Moores. 2014. Conserved mechanisms of microtubule-stimulated ADP release, ATP binding, and force generation in transport kinesins. *eLife.* 3:e03680.
66. Tomishige, M., N. Stuurman, and R. D. Vale. 2006. Single-molecule observations of neck linker conformational changes in the kinesin motor protein. *Nat. Struct. Mol. Biol.* 13:887–894.
67. Asenjo, A. B., and H. Sosa. 2009. A mobile kinesin-head intermediate during the ATP-waiting state. *Proc. Natl. Acad. Sci. USA.* 106:5657–5662.
68. Turner, J., R. Anderson, ..., R. Sakowicz. 2001. Crystal structure of the mitotic spindle kinesin Eg5 reveals a novel conformation of the neck-linker. *J. Biol. Chem.* 276:25496–25502.
69. Kaan, H. Y., V. Ulaganathan, ..., F. Kozielski. 2009. An allosteric transition trapped in an intermediate state of a new kinesin-inhibitor complex. *Biochem. J.* 425:55–60.
70. Goulet, A., W. M. Behnke-Parks, ..., C. A. Moores. 2012. The structural basis of force generation by the mitotic motor kinesin-5. *J. Biol. Chem.* 287:44654–44666.
71. Guan, R., L. Zhang, ..., Z. Chen. 2017. Crystal structure of Zen4 in the apo state reveals a missing conformation of kinesin. *Nat. Commun.* 8:14951.
72. Ramaiya, A., B. Roy, ..., E. Schäffer. 2017. Kinesin rotates unidirectionally and generates torque while walking on microtubules. *Proc. Natl. Acad. Sci. USA.* 114:10894–10899.
73. Nan, X., P. A. Sims, and X. S. Xie. 2008. Organelle tracking in a living cell with microsecond time resolution and nanometer spatial precision. *ChemPhysChem.* 9:707–712.